Acta Astronautica 180 (2021) 370–385

Contents lists available at ScienceDirect

Acta Astronautica

journal homepage: www.elsevier.com/locate/actaastro

Research paper

Hybrid Guardian Map-based adaptive control of spacecraft formation flying on highly elliptical orbits in the restricted three-body problem

Yazan Chihabi *, Steve Ulrich

Department of Mechanical and Aerospace Engineering, Carleton University, Ottawa, Ontario, Canada

ARTICLE INFO

Keywords:
Spacecraft formation flying
Spacecraft relative motion
Spacecraft dynamics
Robust control
Adaptive guidance and control

ABSTRACT

In this paper, a single parameter Guardian Map-based simple adaptive guidance and control architecture for spacecraft formation flying is developed. When compared with traditional vehicles, the dynamics of spacecraft features larger non-linearities, tighter coupling and higher uncertainty as the eccentricity of an orbit increases. In addition, most formation flying applications involve following bounded relative trajectories that are only applicable to circular orbits and hence becomes an unnatural trajectory when used on eccentric orbits, resulting in unnecessary fuel consumption. Making use of a combination of nonlinear Simple Adaptive Control and Guardian Map theories, a novel autonomous adaptive guidance and control system is developed such that the desired closed-loop stability of the system and asymptotic convergence is guaranteed throughout the orbit while tracking fuel-efficient natural trajectories that are applicable to eccentric orbits. Simulation results show various new types and sizes of bounded natural relative orbits to illustrate the increased performance and robustness of the proposed adaptive controller compared to a conventional non-adaptive linear quadratic regulator found in literature.

1. Introduction

Past missions involving the use of multiple spacecraft, such as rendezvous and docking during the Apollo-era, employed a ground-based or pilot input based control architecture. In terms of ground based command and control, the methods usually require a number of engineers to process and calculate the necessary maneuvers, then up-link them to the spacecraft. On the other hand, pilot based guidance and control architectures require human spaceflight which adds its own massive realm of complexities. Among the many applications for spacecraft formation flying are the servicing and maintenance of existing satellites in orbit, and the repair of damaged or otherwise considered obsolete satellites. In a historic, first of its kind mission with Northrop Grumman's spacecraft MEV-1 [1], an Intelsat communications satellite was returned to an operational state in late February 2020.

However, formation flying has many considerations to be taken into account when compared to that of single spacecraft missions. One major consideration is with respect to the guidance and control system, since it is responsible for calculating and controlling the desired relative motion between the spacecraft. Specifically, the chosen control architecture must remain within the desired stability performance for high eccentricity values, and large separation distances while being computationally in-expensive for on-board implementation purposes. Additionally, an accurate guidance system critical to ensure maximum fuel efficiency.

The most common guidance and control method for spacecraft relative motion involves the use of classical control techniques, such as pole-placement and linear quadratic regulator (LQR), designed on the basis of the linear time invariant model formulated by Hill and Clohessy Wiltshire [2]. The LQR is a widely adopted relative motion control scheme for formation flying applications and was flight tested onboard the PRISMA [3] and CanX-4&5 missions [4], for the mode based on formation flying radio frequency (FFRF) sensors and for formation keeping mode, respectively To improve relative motion tracking performance, several formation flying nonlinear control laws were derived, such as ones based on Lyapunov [5] and the feedback linearization techniques [6]. De Queiroz et al. [7] and Wong et al. [8] proposed adaptive state-feedback linearization controllers in which online estimation of unknown parameters and disturbances are employed. More recently, Ulrich [9] proposed a nonlinear passivity-based adaptive control based on decentralized Simple Adaptive Control (DSAC) theory [10]. However, the method proposed by Ulrich requires re-tuning of adaptation rates for different relative motion distances and can become unstable on high orbit eccentricities as a result of the algorithm attempting to adapt control gains responsible for closed-loop

* Corresponding author.
E-mail address: Yazanchihabi@cmail.carleton.ca (Y. Chihabi).

https://doi.org/10.1016/j.actaastro.2020.12.048
Received 24 September 2020; Received in revised form 28 November 2020; Accepted 28 December 2020
Available online 31 December 2020

stability as a result of large variations in nonlinearities over the entire orbit.

To solve the stability issues that arise when developing a control architecture, such as DSAC, on highly elliptical orbits, Guardian Map theory may be utilized. Specifically, the Guardian Map development is based on a new class of eigen-value confinement controllers for linear parameter-varying (LPV) systems, and has been developed for aircraft pitch-rate controllers [11–13] as well as lateral modes of flight [14]. Additionally, it has been used for hypersonic [15–17] and launch vehicle [18] control which features highly nonlinear dynamical models. A few linear parameter varying models of spacecraft relative motion exist in literature [19]; however, to apply Guardian Map theory, the LPV system model must be in polynomial form [20,21] which is the reason as to why the Guardian Map theory has not been applied to spacecraft.

In this context, the main contributions of this paper are: (1) the application of decentralized simple adaptive control ideal model to calculate bounded ideal reference trajectories using relative orbital elements characterized with damping ratio and natural un-damped frequency (2) a new way to describe the dynamics of spacecraft relative motion based on chaser dynamics as an LPV system, and (3) a novel adaptive control law that is robust to changes in orbital position, that is, applicable on highly elliptical orbits by combining the advantages of Guardian Map and DSAC theories.

This paper is organized as follows: Section 2 provides a brief overview of Guardian Map theory, followed by the development of the guidance methodology in Section 3. Section 4 provides a description of nonlinear equations of motion and its LPV derivation in addition to the development of a hybrid Guardian Map nonlinear Simple Adaptive Control law (GSAC). Section 5 presents simulation results for the newly developed controller when compared against a constant gain LQR controller with concluding remarks made in Section 6.

2. Guardian Maps theory

For completeness, this section first provides a brief overview of Guardian Map theory as initially introduced by Saydy et al. [20,21]. This section also provides a new gain calculation procedure which incorporates LQR theory to be used as an initial design point for calculating a set of controller gains. Guardian map theory was initially introduced as a tool for studying the generalized stability of parameterized families of matrices or polynomials. Specifically, generalized stability refers to the confinement of matrix eigenvalues or polynomial zeros to desired regions of the complex plane. In theory, this map is defined as a scalar map for the $n\times n$ matrix which is stable for a region Ω and simultaneously close to this region boundary. In other words, the closed-loop system in question has its respective eigenvalues located at the boundary of a stability region defined by a desired natural frequency and damping ratio. The stability criteria is given by Definitions 1 and 2 [20,21]

Definition 1. Let Ω be an open subset of the complex plane of interest. A system is stable relative to Ω if all eigenvalues of the **A** matrix are located in the $\sigma(\boldsymbol{A})$. This stability set is defined as:

$$S(\Omega) = \left\{ \boldsymbol{A}\in\mathbb{R}^{n\times n} : \sigma(\boldsymbol{A})\subset\Omega \right\} \tag{1}$$

where $\sigma(\boldsymbol{A})$ denotes all the eigenvalues of **A**.

Definition 2. Let ν map $\mathbb{R}^{n\times n}$ into $\mathbb{C}$. Then ν guards $S(\Omega)$ if for all $\boldsymbol{A}\in\bar{S}(\Omega)$, the following holds

$$\nu(\boldsymbol{A}) = 0 \iff \boldsymbol{A}\in\partial S(\Omega) \tag{2}$$

here $\bar{S}$ denotes the closure of the set S and ∂S its boundary.

The three most common Guardian Map regions, shown in Fig. 1), are defined as follows [21]:

1. Stability margin: the open α-shifted left half-plane region (i.e. $Re(z) < \alpha$) is guarded by:

$$\nu_\alpha(\boldsymbol{A}) = det(\boldsymbol{A}\odot\boldsymbol{I} - \alpha\boldsymbol{I}\odot\boldsymbol{I})det(\boldsymbol{A} - \alpha\boldsymbol{I}) \tag{3}$$

   where $\odot$ is the bialternate product . (See [20,21]) A simplified case of negative margin is Hurwitz stability where $\alpha = 0$.
2. The damping stability is a cone shaped region with a half angle of $\theta = cos^{-1}(\zeta)$ guarded by:

$$\nu_\zeta(\boldsymbol{A}) = det(\boldsymbol{A}^2\odot\boldsymbol{I} + (1-2\zeta^2)\boldsymbol{A}\odot\boldsymbol{A})det(\boldsymbol{A}) \tag{4}$$

3. The Schur Stability region is a circular region defined by radius ω_n guarded by:

$$\nu_{\omega_n}(\boldsymbol{A}) = det(\boldsymbol{A}\odot\boldsymbol{A} - \omega_n^2\boldsymbol{I}\odot\boldsymbol{I})det(\boldsymbol{A} - \omega_n\boldsymbol{I})det(\boldsymbol{A} + \omega_n^2\boldsymbol{I}) \tag{5}$$

4. The Guardian Map ν_Ω is then found by:

$$\nu_\Omega(\boldsymbol{A}) = \nu_\alpha(\boldsymbol{A})\nu_\zeta(\boldsymbol{A})\nu_{\omega_n}(\boldsymbol{A}) \tag{6}$$

2.1. Robust stability and the characterization of stabilizing gains

Let $\{\boldsymbol{A}(r) : r \in U \subset \mathbb{R}^k\}$ be a continuous family of $n\times n$ matrices which depend on the parameter vector $r := (r_1,\dots,r_k)$ where each parameter lies in a given range for which only the bounds are known, say $\{r \in U \subset \mathbb{R}^k\}$ [21].

Theorem II.1. *Let $S(\Omega)$ be guarded by the map ν_Ω. $\{\boldsymbol{A}(r) : r \in U\}$ is stable relative to Ω if and only if*

1. *it is nominally stable, i.e. $\boldsymbol{A}(r_0) \in S(\Omega)$ for some $r_0 \in U$; and,*
2. *$\nu_\Omega(\boldsymbol{A}(r)) \neq 0$, for all $r \in U$.*

Corollary II.1. *Let $S(\Omega)$ be guarded by the map ν and consider the family $\{\boldsymbol{A}(r) : r \in U\}$. Then the set C defined by:*

$$C = r \in \mathbb{R}^k : \nu_\Omega(\boldsymbol{A}(r)) = 0 \tag{7}$$

divides the parameter space $\mathbb{R}^k$ into components C_i that are either stable or unstable relative to Ω. To see which situation prevails for a given component C_i, one simply has to test $\boldsymbol{A}(r)$ for any one vector in C_i.

2.2. Robust stability: One-parameter family stability test

In the problem this paper addresses, the dynamical model is derived as linear parameter varying state–space model depending on the distance with respect to a primary body. As such, only one-parameter families of real matrices relative to domain Ω is considered and is given in the form of [20,21]

$$\boldsymbol{A}(r) = \boldsymbol{A}_0 + r\boldsymbol{A}_1 + \cdots + r^k\boldsymbol{A}_k \tag{8}$$

with $\boldsymbol{A}_i$ given constant matrices, and such that $\boldsymbol{A}(r_0)$ is stable in Ω. The corresponding Guardian Map $\nu_\Omega[\boldsymbol{A}(r)]$ is a polynomial in r. Let

1. $r^- \triangleq sup\{r < r_0 : \nu_\Omega[\boldsymbol{A}(r)] = 0\}$ (or $-\infty$ if none exist)
2. $r^+ \triangleq inf\{r > r_0 : \nu_\Omega[\boldsymbol{A}(r)] = 0\}$ (or $+\infty$ if none exist)

be the maximal perturbation bounds for non singularity of matrices around $r = r_0$. In other words, this means that the system represented by Eq. (8) is robust to the changes in parameter r if it is varied from r^- to r^+, where r_0 lies in between the upper and lower limits. The following Lemma puts this into context.

Lemma II.1. *Let $\boldsymbol{A}(r) = \boldsymbol{A}_0 + r\boldsymbol{A}_1 + \cdots + r^k\boldsymbol{A}_k$ be a polynomial matrix in uncertain parameter r real with given constant matrices $\boldsymbol{A}_i$, such that $\boldsymbol{A}(r_0)$ is stable with respect to Ω, and let $S(\Omega)$ be guarded by a map ν_Ω. Then, $\boldsymbol{A}(r)$ is stable relative to Ω for all $r \in (r^-, r^+)$. Furthermore, this interval is the largest one containing r_0.*

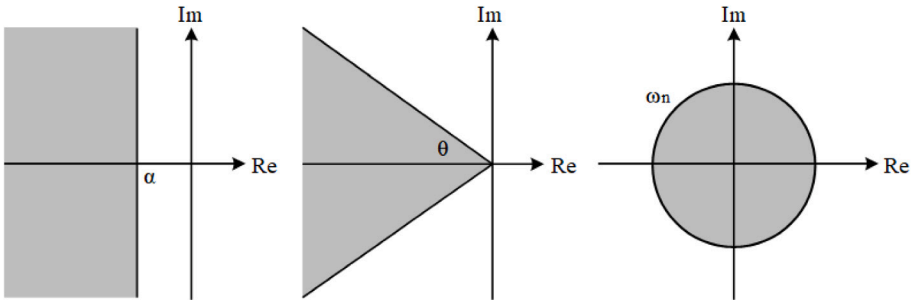

Fig. 1. Stability regions.

2.3. Gain calculation procedure

The original procedure for the gain selection can be found in [21]. For the application in this paper, the procedure is slightly modified to improve robustness. Specifically, the initial controller gains is selected using the LQR method and converted into a set of PD gains. This is done by selecting a set of initial LQR weighting matrices and then extracting the diagonal elements contained within the resulting gain matrix which are then used as the initial set of controller gains. However, the limitation of this initial gain calculation method is that the PD gains can only be extracted from systems with the same number of inputs as the number of equations defining the states This way, the Guardian Map can deliver the same performance results as an LQR controller over the entire stability interval. In other words, this method ensures the robustness of the optimal controller. The new procedure is provided as follows:

1. Initialization: Let Ω be a region of the complex plane; ν_Ω be a corresponding Guardian Map; and $\boldsymbol{A}(r, \boldsymbol{K})$ be a closed-loop matrix, depending polynomially on the single parameter $r \in [r_{min}, r_{max}]$ and the gain vector $\boldsymbol{K} = [K_j] \in \mathbb{R}^k$. Obtain a controller $\boldsymbol{K}^0$ using the LQR designed for the nominal case $r_0 = r_{min}$, then using the eigen-values of the initial closed-loop system define the stability region Ω. Set $n = 0$. Using the Lemma shown previously on $\boldsymbol{A}(r, \boldsymbol{K}^0)$, find the largest stability interval $]\underline{r}_0, \bar{r}_0[$ containing r_0. If $\bar{r}_0 > r_{max}$, then Stop, else set the counter $n = n+1$
2. Synthesis phase: Find a new gain vector $\boldsymbol{K}^n$ inside a component defined by $\nu_\Omega(\bar{r}_{n-1}, \boldsymbol{K}) = 0$ using the search algorithm provided in Fig. 2 with an initial vector $\boldsymbol{K}^{n-1}$.
3. Robustness Analysis: Using Lemma shown previously on $\boldsymbol{A}(r, \boldsymbol{K}^n)$, find the largest stability interval $]\underline{r}_n, \bar{r}_n[$ containing $\bar{r}_{n-1}$. If $\bar{r}_n > r_{max}$, then go to Final Step or Stop, else set the counter $n = n + 1$ and go to step 2.
4. Interpolation: If an interpolation $\boldsymbol{K} = \boldsymbol{K}(r)$ is sought, use the Lemma to check if stability is preserved for all $r \in [r_{min}, r_{max}]$.

3. Formation flying guidance methodology

Most relative motion guidance and control methods involve the use of Hill's linearized equations of motion to design relative trajectories such as projected circular motion or in-plane elliptical formation. However, using those equations for spacecraft that are on a highly elliptical orbit results in large amounts of actuation to force the chaser spacecraft to follow the desired relative trajectory.

This section presents a novel guidance methodology that combines SAC theory with spacecraft relative dynamics in terms of relative orbital elements. Specifically, the guidance law constructs ideal relative trajectories that display transient and steady-state time responses based on desired relative orbital elements, damping and natural frequencies.

3.1. Natural orbital elements-based relative motion

For completeness, the equations of motion used in the computation of the desired relative motion is presented in this section. Specifically, the desired trajectory is computed using Schaub's linearized equations of motion [22, p. 593–673]. The equations are derived using a first order approximation of Gurfil and Kholshevnikov's equations [23,24] such that the relative position is computed in closed form as a function of relative orbital elements. The advantage of this method is that the equations are valid for an arbitrary eccentric orbit and can be made to include orbital perturbations for increased accuracy and efficiency [25, 26]. The equations are presented in state–space form as

$$\boldsymbol{\rho} = \begin{bmatrix} x & y & z \end{bmatrix}^T = \boldsymbol{F}\,\Delta\boldsymbol{\alpha e} \tag{9}$$

where

$$\boldsymbol{\rho} = \boldsymbol{r}_c - \boldsymbol{r}_t \tag{10}$$

$$\boldsymbol{\alpha e} = \begin{bmatrix} a & e & i & \omega & \Omega & M \end{bmatrix}^T \tag{11}$$

$$\boldsymbol{F} = \begin{bmatrix} \frac{r_t}{a_t} & -a_t\cos\theta_t & 0 & 0 & 0 & \frac{a_t e_t \sin\theta_t}{\sqrt{1-e_t^2}} \\ 0 & \frac{r_t \sin\theta_t}{1-e_t^2}(2+e_t\cos\theta_t) & 0 & r_t & r_t\cos i_t & \frac{r_t}{(1-e_t^2)^{3/2}} \\ 0 & 0 & r_t\sin\theta_t & 0 & -r_t\cos\theta_t\sin\theta_t & 0 \end{bmatrix} \tag{12}$$

$\boldsymbol{r}_c$ and $\boldsymbol{r}_t$ denote the position vectors of the chaser and target spacecraft expressed in the LVLH reference frame with respect to the primary body, and $\boldsymbol{\rho}$ is the relative position vector of the chaser with respect to the target expressed in the LVLH reference frame. The variable $\Delta\boldsymbol{\alpha e}$ contains the difference in classical orbital elements between the chaser and the target spacecraft such that $\Delta\boldsymbol{\alpha e} = \boldsymbol{\alpha e}_c - \boldsymbol{\alpha e}_t$, where the subscripts c and t denote the chaser and target, respectively. The variables a, e, i, ω, Ω and M denote the semi-major axis, eccentricity, inclination, argument of perigee, right ascension of the ascending node and mean anomaly, respectively. This allows for the analytical calculation of bounded natural relative trajectories by carefully selecting a set of relative orbital elements that defines the formation geometry. For example, a natural in-plane elliptical formation trajectory can be calculated by selecting a relative eccentricity while keeping the other five as zero. The target's orbital radius magnitude, r_t, is calculated using the orbit equation as

$$r_t = \frac{a_t(1-e_t^2)}{1+e_t\cos\theta_t} \tag{13}$$

where θ_t is the target's true anomaly. Since the equations shown above are functions of the true anomaly, θ, a way of computing it is required. The true anomaly can be calculated using the eccentric anomaly and mean anomaly using the simple recursive solution given by [27]

$$E = M + e\sin(M + e\sin(M + e\sin(M + \cdots + e\sin(M)))) \tag{14}$$

$$\cos\theta = \frac{\cos E - e}{1 - e\cos E} \tag{15}$$

$$\sin\theta = \frac{\sqrt{1-e^2}\sin E}{1 - e\cos E} \tag{16}$$

0. **Initialization.**
Let Ω and $\boldsymbol{K}^0 \in \mathbb{R}^p$, such that $\nu_\Omega(\boldsymbol{K}^0) = 0$ and n are the maximum desired number of main loop iterations.
Set the counter $m \leftarrow 0$.
1. **Main loop.**
While $m \leq n$
For i from one to p
a) Fix all the gains $\boldsymbol{K}$ to their current values except K_i.
b) The guardian map $\nu_\Omega(\boldsymbol{K})$ now only depends on K_i.
c) Using Lemma II.1, find the largest stability interval $]\underline{K}_i, \bar{K}_i[$ containing K_i^m.
d) Set $K_i^{m+1} \leftarrow (\underline{K}_i + \bar{K}_i)/2$.
End
A new gain vector $\boldsymbol{K}^{m+1}$ is then obtained.
a) If $\|\boldsymbol{K}^m - \boldsymbol{K}^{m+1}\| \leq \epsilon_K(1 + \|\boldsymbol{K}^m\|)$ (with ϵ_K arbitrary small positive value), then **Stop**.
b) Else, set $m \leftarrow m + 1$.
End

Fig. 2. Search algorithm [21].

$$\theta = \tan^{-1}\frac{\sin\theta}{\cos\theta} \tag{17}$$

where E is the eccentric anomaly. This is a recursive solution based on the well-known Newton–Raphson Iteration Technique which implies an infinite series and is used to solve nonlinear equations which cannot be solved analytically [28]. Therefore, a term will become truncated based on the desired accuracy. The mean anomaly can be found by

$$M = M_0 + \dot{M}(t - t_0) \tag{18}$$

$$\dot{M} = n = \sqrt{\frac{\mu}{a^3}} \tag{19}$$

where μ is the gravitational constant of the primary body, n is the mean orbital motion, t is the current time in seconds and t_0 is the initial time of M_0.

3.2. Output feed-back guidance law

Inspired by SAC theory [27], the overshoots and oscillations that arise from commanding a spacecraft to follow a relative trajectory can be reduced by employing the novel use of an ideal LTI state–space model given as

$$\dot{\boldsymbol{x}}_m = \boldsymbol{A}_m\boldsymbol{x}_m + \boldsymbol{B}_m\boldsymbol{u}_m \tag{20}$$

$$\boldsymbol{y}_m = \boldsymbol{C}_m\boldsymbol{x}_m \tag{21}$$

where

$$\boldsymbol{x}_m = \begin{bmatrix}\boldsymbol{\rho}_m^T & \dot{\boldsymbol{\rho}}_m^T\end{bmatrix}^T = \begin{bmatrix}x_m & y_m & z_m & \dot{x}_m & \dot{y}_m & \dot{z}_m\end{bmatrix}^T \tag{22}$$

$$\boldsymbol{y}_m = \begin{bmatrix}\lambda x_m + \dot{x}_m & \lambda y_m + \dot{y}_m & \lambda z_m + \dot{z}_m\end{bmatrix}^T \tag{23}$$

$$\boldsymbol{u}_m = \boldsymbol{\rho}_d = \begin{bmatrix}x_d & y_d & z_d\end{bmatrix}^T \tag{24}$$

where $\boldsymbol{\rho}_d$ denotes the desired relative position of chaser spacecraft, as defined by Eq. (9), and $\boldsymbol{x}_m$ denotes the ideal states.

The constant λ is a positive-definite scaling gain which is used in the development of simple adaptive control methodologies [9,10]. Specifically, in SAC theory, the dimension of the output $\boldsymbol{y}$ must be equal to the number of control inputs present within the which ensures that the system is Almost Strictly Passive (ASP). ASP for nonlinear systems means that the dynamics is: (1) strictly minimum phase (zero dynamics is stable), and (2) the product $\boldsymbol{CB}$ is positive definite symmetric (i.e: square system). Furthermore, the ASP property is crucial to the development of SAC as it is required prove the asymptotic stability of the adaptive controller. For the case of spacecraft relative motion, the output signal can be constructed by taking a linear combination of a scaled position and velocity, since there are six states and three controller inputs. The reason the a scaling gain is present for the position is because the signal is a combination of two different units, and hence the position unit must include scaling which is arbitrarily chosen through trial and error.

The desired closed-loop relative motion response to these inputs is characterized through the ideal model matrices $\boldsymbol{A}_m$, $\boldsymbol{B}_m$ and $\boldsymbol{C}_m$ given as

$$\boldsymbol{A}_m = \begin{bmatrix} 0 & 0 & 0 & 1 & 0 & 0 \\ 0 & 0 & 0 & 0 & 1 & 0 \\ 0 & 0 & 0 & 0 & 0 & 1 \\ -\omega_n^2 & 0 & 0 & -2\zeta\omega_n & 0 & 0 \\ 0 & -\omega_n^2 & 0 & 0 & -2\zeta\omega_n & 0 \\ 0 & 0 & -\omega_n^2 & 0 & 0 & -2\zeta\omega_n \end{bmatrix} \tag{25}$$

$$\boldsymbol{B}_m = \begin{bmatrix} 0 & 0 & 0 & \omega_n^2 & 0 & 0 \\ 0 & 0 & 0 & 0 & \omega_n^2 & 0 \\ 0 & 0 & 0 & 0 & 0 & \omega_n^2 \end{bmatrix}^T \tag{26}$$

$$\boldsymbol{C}_m = \begin{bmatrix}\lambda\boldsymbol{I}_3 & \boldsymbol{I}_3\end{bmatrix} \tag{27}$$

where ζ and ω_n are defined by the Guardian Map in Eqs. (4) and (5).

4. Hybrid Guardian Map simple adaptive control methodology in the simplified three-body problem

In this application, the chaser spacecraft provides the actuation to follow a controlled motion. Therefore, the system dynamics can be represented by the simplified three-body dynamical model of a spacecraft relating inertial acceleration, $\ddot{\vec{r}}_c$, to position of the spacecraft along its respective orbit $\vec{r}_c$ [29, p. 69]

$$\ddot{\vec{r}}_c = -\frac{\mu}{r_c^3}\vec{r}_c - \frac{\mu'}{r'^3}\vec{r}_c + \vec{u}_c + G\left(\vec{r}_c, \dot{\vec{r}}_c\right) \tag{28}$$

where $\vec{u}_c$ denotes the control acceleration provided by the chaser, $G\left(\vec{r}_c, \dot{\vec{r}}_c\right)$ is a vector containing perturbing nonlinear effects that are dependent on the spacecraft's states, and $r_c = |\vec{r}_c|$. The third body effects are contained in the term with third body gravitational constant, μ', and the radial distance of the third body with respect to the primary body, r', which can be calculated as

$$r' = \frac{a'(1 - e'^2)}{1 + e'\cos(\theta')} \tag{29}$$

where $'$ denotes the orbital elements and parameters of the third body. Expressed as components in the LVLH reference frame Eq. (28) becomes

$$\ddot{\boldsymbol{r}}_{c_L} = -\left(\frac{\mu}{r_c^3} + \frac{\mu'}{r'^3}\right)\boldsymbol{r}_{c_L} + \boldsymbol{u}_{c_L} + \boldsymbol{G}\left(\boldsymbol{r}_{c_L}, \dot{\boldsymbol{r}}_{c_L}\right) \tag{30}$$

where $\ddot{\boldsymbol{r}}_{c_L}$, $\boldsymbol{r}_{c_L}$, and $\boldsymbol{u}_{c_L}$ are the acceleration and position vector components of the chaser spacecraft and control acceleration expressed in the LVLH reference frame. The use of Guardian Map theory is limited to classical stability analysis techniques and does not guarantee asymptotic convergence of states on its own. As mentioned previously, employing the use of Simple Adaptive Control techniques to control

a chaser spacecraft on a highly elliptical orbit results in instability of the controller. Selecting a slightly modified version of simple adaptive control methodology [30], such that a proportional-derivative term is included to control the ideal states and maintain the stability of the system according to Guardian Maps theory [20,21] results in the following control architecture

$$\boldsymbol{u}_{c_L} = K_p \boldsymbol{e}_m + K_d \dot{\boldsymbol{e}}_m + \boldsymbol{K}_x(t)\boldsymbol{x}_m + \boldsymbol{K}_u(t)\boldsymbol{u}_m \tag{31}$$

where K_p and K_d denote the scalar proportional and derivative gains. The matrices $\boldsymbol{K}_x(t) \in \mathbb{R}^{3\times 6}$ and $\boldsymbol{K}_u(t) \in \mathbb{R}^{3\times 3}$ denote passivity-based adaptive feed-forward control gains which do not contribute to the systems closed-loop stability but ensures asymptotic convergence of the states. Collectively, this control law is titled as "Guardian Map Simple Adaptive Control (GSAC) Law". The error $\boldsymbol{e}$ and its derivative are given as

$$\boldsymbol{e} = \boldsymbol{r}^d_{c_L} - \boldsymbol{r}^a_{c_L} \tag{32}$$

$$\dot{\boldsymbol{e}} = \dot{\boldsymbol{r}}^d_{c_L} - \dot{\boldsymbol{r}}^a_{c_L} \tag{33}$$

where the superscripts d and a denote the desired and actual components. Applying Eq. (10) to Eq. (32) yields

$$\boldsymbol{e} = (\boldsymbol{\rho}^d_L + \boldsymbol{r}^d_{t_L}) - (\boldsymbol{\rho}^a_L + \boldsymbol{r}^a_{t_L}) \tag{34}$$

where $\boldsymbol{\rho}_L$ denotes the relative position vector components of the chaser spacecraft with respect to the target expressed in LVLH. The desired and actual target positions are one and the same, i.e.: $\boldsymbol{r}^d_{t_L} = \boldsymbol{r}^a_{t_L} = \boldsymbol{r}_{t_L}$ which results in

$$\boldsymbol{e} = \boldsymbol{\rho}^d_L - \boldsymbol{\rho}^a_L \tag{35}$$

The same can be shown for the error derivative $\dot{\boldsymbol{e}}$. Therefore, it has been shown that the system dynamics can be represented by Eq. (28). Equivalently, the errors $\boldsymbol{e}_m$ and $\dot{\boldsymbol{e}}_m$ can be defined as

$$\boldsymbol{e}_m = \boldsymbol{\rho}_m - \boldsymbol{\rho}^a_L \tag{36}$$

$$\dot{\boldsymbol{e}}_m = \dot{\boldsymbol{\rho}}_m - \dot{\boldsymbol{\rho}}^a_L \tag{37}$$

4.1. LPV state–space model and adaptive control formulation

To apply the Guardian Map theory, the system dynamics must be represented as an LPV system of a family polynomial matrices given by Eq. (8). The nonlinear dynamics represented by Eq. (28) is therefore herein expressed as an LPV system by defining $\beta \triangleq -(\mu/r_c^3 + \mu'/r'^3)$. Then, the system dynamics including the proposed control law is represented as:

$$\dot{\boldsymbol{x}}_{c_L} = \boldsymbol{A}(\beta, K_p, K_d)\boldsymbol{x}_{c_L} + \boldsymbol{B}\left(\boldsymbol{K}_x(t)\boldsymbol{x}_m + \boldsymbol{K}_u(t)\boldsymbol{u}_m\right) + \boldsymbol{G}\left(\boldsymbol{x}_{c_L}\right) \tag{38}$$

where $\boldsymbol{x}_{c_L} = \begin{bmatrix}\boldsymbol{r}^T_{c_L} & \dot{\boldsymbol{r}}^T_{c_L}\end{bmatrix}^T$, $\boldsymbol{A}(\beta, K_p, K_d) = \boldsymbol{A}_0(K_p, K_d) + \boldsymbol{A}_1(\beta)$ and the matrix $\boldsymbol{B}$ is given by

$$\boldsymbol{B} = \begin{bmatrix}0 & 0 & 0 & 1 & 0 & 0\\ 0 & 0 & 0 & 0 & 1 & 0\\ 0 & 0 & 0 & 0 & 0 & 1\end{bmatrix}^T \tag{39}$$

The system represented by Eq. (38) is independent of unknown chaser mass. As described in the previous section, the feed-forward gains do not contribute to the stability of the system and therefore only $\boldsymbol{A}(\beta, K_p, K_d)$ is necessary to apply Guardian Map theory. The matrices $\boldsymbol{A}_0(K_p, K_d)$ and $\boldsymbol{A}_1(\beta)$ are defined as

$$\boldsymbol{A}_0(K_p, K_d) = \begin{bmatrix}0 & 0 & 0 & 0 & 0 & 0\\ 0 & 0 & 0 & 0 & 0 & 0\\ 0 & 0 & 0 & 0 & 0 & 0\\ -K_p & 0 & 0 & -K_d & 0 & 0\\ 0 & -K_p & 0 & 0 & -K_d & 0\\ 0 & 0 & -K_p & 0 & 0 & -K_d\end{bmatrix} \tag{40}$$

$$\boldsymbol{A}_1(\beta) = \begin{bmatrix}0 & 0 & 0 & 1 & 0 & 0\\ 0 & 0 & 0 & 0 & 1 & 0\\ 0 & 0 & 0 & 0 & 0 & 1\\ \beta & 0 & 0 & 0 & 0 & 0\\ 0 & \beta & 0 & 0 & 0 & 0\\ 0 & 0 & \beta & 0 & 0 & 0\end{bmatrix} \tag{41}$$

Using the matrices defined above, adaptive control gains as a function of parameter β can be determined by the gain-calculation procedure in Section 2.3 with the LPV model in Eq. (38) which ensures the robust stability of the control law in Eq. (31) over the entire orbit. The control law, incorporating the Guardian Map adaptive gains, can be rewritten as

$$\boldsymbol{u}_{c_L} = \boldsymbol{K}(\beta, t)\boldsymbol{r} \tag{42}$$

$$\boldsymbol{r} = \begin{bmatrix}\boldsymbol{e}^T_m & \dot{\boldsymbol{e}}^T_m & \boldsymbol{x}^T_m & \boldsymbol{u}^T_m\end{bmatrix}^T \tag{43}$$

where

$$\boldsymbol{K}(\beta, t) = \begin{bmatrix}\boldsymbol{K}_{PD}(\beta) & \boldsymbol{K}_x(t) & \boldsymbol{K}_u(t)\end{bmatrix} \tag{44}$$

$$\boldsymbol{K}_{PD}(\beta) = \begin{bmatrix}K_p(\beta) & 0 & 0 & K_d(\beta) & 0 & 0\\ 0 & K_p(\beta) & 0 & 0 & K_d(\beta) & 0\\ 0 & 0 & K_p(\beta) & 0 & 0 & K_d(\beta)\end{bmatrix} \tag{45}$$

The feed-forward gains $\boldsymbol{K}_x(t)$ and $\boldsymbol{K}_u(t)$ are derived in the following subsection.

4.2. Passivity-based adaptive feed-forward law

The adaptive feed-forward gains $\boldsymbol{K}_x(t)$ and $\boldsymbol{K}_u(t)$ can be computed according to decentralized Simple Adaptive Control methodology by splitting the gains into proportional and integral gains [10] as

$$\boldsymbol{K}_x(t) = \boldsymbol{K}_{Px}(t) + \boldsymbol{K}_{Ix}(t) \tag{46}$$

$$\boldsymbol{K}_u(t) = \boldsymbol{K}_{Pu}(t) + \boldsymbol{K}_{Iu}(t) \tag{47}$$

where the proportional terms, $\boldsymbol{K}_{Px}$ and $\boldsymbol{K}_{Pu}$ within the equations defined above are known to increase the rate of asymptotic convergence [9]. Specifically, the direct feed-forward adaptation law calculates the integral terms of these gains to achieve a steepest descent minimization of the tracking errors. The adaptation mechanism is given as [31]

$$\dot{\boldsymbol{K}}_{Ix}(t) = \boldsymbol{R}^T diag\{\boldsymbol{R}\boldsymbol{e}_y\boldsymbol{x}^T_m\}\Gamma_{Ix} \tag{48}$$

$$\boldsymbol{K}_{Px}(t) = \boldsymbol{R}^T diag\{\boldsymbol{R}\boldsymbol{e}_y\boldsymbol{x}^T_m\}\Gamma_{Px} \tag{49}$$

$$\dot{\boldsymbol{K}}_{Iu}(t) = diag\{\boldsymbol{e}_y\boldsymbol{u}^T_m\}\Gamma_{Iu} \tag{50}$$

$$\boldsymbol{K}_{Pu}(t) = diag\{\boldsymbol{e}_y\boldsymbol{u}^T_m\}\Gamma_{Pu} \tag{51}$$

with

$$\boldsymbol{R} = \begin{bmatrix}\boldsymbol{I}_3 & \boldsymbol{I}_3\end{bmatrix}^T \in \mathbb{R}^{6\times 3} \tag{52}$$

$$\boldsymbol{e}_y = \boldsymbol{y}_m - \boldsymbol{y} \tag{53}$$

where $\Gamma_{Ix}, \Gamma_{Px} \in \mathbb{R}^{6\times 6}$ and $\Gamma_{Iu}, \Gamma_{Pu} \in \mathbb{R}^{3\times 3}$ denote the positive definite diagonal matrices that set the adaptation rate of the feed-forward adaptive gains, that is, the rate at which the gains are allowed to vary.

4.3. Lyapunov stability of the adaptive controller

Perfect tracking is obtained when the plant matches the ideal model, which implies that it has a bounded trajectory equivalent to the ideal states, denoted by $\boldsymbol{x}^*$. Through the use of Lyapunov direct methods, the asymptotic convergence of the controller can be proven [32]. Specifically, representing the ideal plant dynamics as

$$\dot{\boldsymbol{x}}^* = \boldsymbol{A}^*_1\boldsymbol{x}^* + \boldsymbol{B}\boldsymbol{u}^* + \boldsymbol{G}^* \tag{54}$$

$$\boldsymbol{y}_m = \boldsymbol{C}\boldsymbol{x}^* \tag{55}$$

with

$$\boldsymbol{u}^* = \tilde{\boldsymbol{K}}_x \boldsymbol{x}_m + \tilde{\boldsymbol{K}}_u \boldsymbol{u}_m \tag{56}$$

where $\tilde{\boldsymbol{K}}_x \in \mathbb{R}^{3\times6}$ and $\tilde{\boldsymbol{K}}_u \in \mathbb{R}^{3\times3}$ are constant ideal feed-forward control gains, which are only used to prove asymptotic stability of the feed-forward controller. The plant dynamics represented by Eq. (54) has a trajectory equivalent to $\boldsymbol{x}^*$ with $\boldsymbol{A}_1^* = \boldsymbol{A}_1(\beta^*)$ and $\boldsymbol{G}^* = \boldsymbol{G}(\boldsymbol{x}^*)$ while in Eq. (56), $\boldsymbol{u}^*$ denotes the ideal control input (with constant feed-forward gains) obtained when perfect tracking occurs ($\boldsymbol{e}_y = \boldsymbol{0}_3$). Otherwise, there is a non-zero state error defined as [9,10]

$$\boldsymbol{e}_x = \boldsymbol{x}^* - \boldsymbol{x} \tag{57}$$

where

$$\boldsymbol{x} = \begin{bmatrix} \rho_L^a & \dot{\rho}_L^a \end{bmatrix} \tag{58}$$

Following a similar logic, $\boldsymbol{e}_y$ is no longer equal to zero and is defined as

$$\boldsymbol{e}_y = \boldsymbol{C}\boldsymbol{x}^* - \boldsymbol{C}\boldsymbol{x} = \boldsymbol{C}\boldsymbol{e}_x \tag{59}$$

To prove the asymptotic stability of the controller, a continuously differentiable positive-definite Lyapunov function candidate is selected as

$$V = \boldsymbol{e}_x^T \boldsymbol{P} \boldsymbol{e}_x + tr\left\{ \left(\boldsymbol{K}_I(t) - \tilde{\boldsymbol{K}}\right) \Gamma_I^{-1} \left(\boldsymbol{K}_I(t) - \tilde{\boldsymbol{K}}\right)^T \right\} \tag{60}$$

where

$$\boldsymbol{K}_I(t) = \begin{bmatrix} \boldsymbol{K}_{Ix}(t) & \boldsymbol{K}_{Iu}(t) \end{bmatrix} \tag{61}$$

$$\tilde{\boldsymbol{K}} = \begin{bmatrix} \tilde{\boldsymbol{K}}_x & \tilde{\boldsymbol{K}}_u \end{bmatrix} \tag{62}$$

$$\Gamma_I = \begin{bmatrix} \Gamma_{Ix} & \boldsymbol{0}_{6\times3} \\ \boldsymbol{0}_{3\times6} & \Gamma_{Iu} \end{bmatrix} \tag{63}$$

and $tr\{\}$ denotes the trace function. The time derivative of the Lyapunov function is herein derived as

$$\begin{aligned} \dot{V} = & -\boldsymbol{e}_x^T \boldsymbol{Q} \boldsymbol{e}_x \\ & - 2\boldsymbol{e}_x^T \boldsymbol{C}^T \boldsymbol{S}^T diag\{\boldsymbol{S}\boldsymbol{e}_y \boldsymbol{r}_{ff}^T\} \Gamma_P \boldsymbol{r}_{ff} \\ & + 2\boldsymbol{e}_x^T \boldsymbol{P} \left[\left(\boldsymbol{A}_1^* - \boldsymbol{A}_1\right) \boldsymbol{x}^* + \left(\boldsymbol{G}^* - \boldsymbol{G}\right) \right] \end{aligned} \tag{64}$$

where

$$\boldsymbol{r}_{ff} = \begin{bmatrix} \boldsymbol{x}_m^T & \boldsymbol{u}_m^T \end{bmatrix}^T \tag{65}$$

$$\Gamma_P = \begin{bmatrix} \Gamma_{Px} & \boldsymbol{0}_{6\times3} \\ \boldsymbol{0}_{3\times6} & \Gamma_{Pu} \end{bmatrix} \tag{66}$$

$$\boldsymbol{S} = \begin{bmatrix} \boldsymbol{I}_3 & \boldsymbol{I}_3 & \boldsymbol{I}_3 \end{bmatrix}^T \in \mathbb{R}^{9\times3} \tag{67}$$

$$\boldsymbol{Q} = -\left(\dot{\boldsymbol{P}} + \boldsymbol{P}\boldsymbol{A}(\beta, K_p, K_d) + \boldsymbol{A}^T(\beta, K_p, K_d)\boldsymbol{P} \right) \tag{68}$$

$\boldsymbol{P}$ and $\boldsymbol{Q}$ are positive definite matrices. In order to prove the asymptotic convergence of the adaptive controller, the Lyapunov derivative function of Eq. (64) must be negative definite (i.e.: $\dot{V} < 0$). The Lyapunov derivative function of Eq. (64) is negative definite in $\boldsymbol{e}_x$ and negative semi-definite in $\left[\boldsymbol{e}_x, \boldsymbol{K}_I(t)\right]$ if and only if

$$2\boldsymbol{e}_x^T \boldsymbol{P} \left[\left(\boldsymbol{A}_1^* - \boldsymbol{A}_1\right) \boldsymbol{x}^* + \left(\boldsymbol{G}^* - \boldsymbol{G}\right) \right] = 0 \tag{69}$$

is equal to zero. This condition is satisfied when the states $\boldsymbol{x}$ eventually match the ideal states $\boldsymbol{x}^*$ [30]. In turn, the fulfillment of this condition implies that $\boldsymbol{A}_1 = \boldsymbol{A}_1^*$ and $\boldsymbol{G} = \boldsymbol{G}^*$. Finally, asymptotic convergence of the tracking errors can be proven by invoking LaSalle's invariance principle for non-autonomous systems [30,33]. Specifically, all system trajectories are contained within domain $\Xi_0 = \left\{ \left[\boldsymbol{e}_x, \boldsymbol{K}_I(t)\right] | V\left(\left[\boldsymbol{e}_x, \boldsymbol{K}_I(t)\right], t\right) \leq V\left(\left[\boldsymbol{e}_{x_0}, \boldsymbol{K}_{I_0}(t)\right], 0\right) \right\}$ (where the subscript $\{\}_0$ denotes the initial conditions) [9,10]. The state–space $\left[\boldsymbol{e}_x, \boldsymbol{K}_I(t)\right]$ ultimately reaches the domain defined by $V\left(\left[\boldsymbol{e}_x, \boldsymbol{K}_I(t)\right], t\right) = 0$, i.e.: $\Xi_f = \Xi_0 \subset \Xi$, where Ξ denotes the domain defined by the Lyapunov derivative identical to zero [34]. Since $\dot{V}\left(\left[\boldsymbol{e}_x, \boldsymbol{K}_I(t)\right], t\right)$ is negative definite in $\boldsymbol{e}_x$, the system ends with $\boldsymbol{e}_x = 0$ and this implies $\boldsymbol{e}_y = \boldsymbol{C}\boldsymbol{e}_x = \boldsymbol{0}_3$, resulting in the guaranteed asymptotic stability of the state and output tracking errors.

5. Numerical simulations

This section presents a comparison of performance between the adaptive guidance and control architecture and an LQR controller that tracks a standard desired trajectory as defined by Eq. (9). The numerical propagator used in all simulation results presented here integrates the inertial two-body equation of motion to which the inertial perturbing accelerations are added. Specifically, perturbing accelerations due to gravitational field through the expansion of gravitational potential function up to degree and order 180 [35], third body effects of the sun, moon and solar system planets [36,37], ocean and solid Earth tidal effects, relativity [35], solar radiation pressure, and drag were calculated [38]. Tracking error and control inputs were compared for slightly elliptical LEO and HEO formations. Furthermore, a sensitivity analysis of the newly developed control law is performed by varying eccentricity and formation size. The proposed guidance and control system was evaluated for an in-plane elliptical formation using Eq. (9) as an ideal model and compared against using Hill's equations A total of four cases were analyzed: (1) The proposed guidance and control system was evaluated for an in-plane elliptical formation using Eq. (9) as an ideal model and compared against using Hill's equations, (2) the three controllers previously described, including the proposed control law, are compared against each other on an arbitrary highly elliptical orbit, (3) European Space Agency's Proba-3 mission [39], and (4) a hypothetical formation flying mission around the tumbling Alouette-2 spacecraft (one of Canada's early satellites launched into orbit.

For the drag model, it is assumed that both spacecraft maximum surface area is always perpendicular to the flow direction and that the atmosphere rotates with the Earth, and constant coefficient of drag for both spacecraft of 2.3 is assumed. The mass and surface area, arbitrarily chosen, are 20 kg and 1 m^2, and 30 kg and 2 m^2 for the chaser and target spacecraft respectively. These values are used for cases 1 and 2 presented in the following subsections. For the Proba-3 case, the mass and surface area are 211 kg and 1.77 m^2, and 339 kg and 3.34 m^2 for the chaser and target spacecraft, respectively. The final case, concerning Alouette-2, was initialized with the mass and surface area are 146.5 kg and 2 m^2, and 200 kg and 3 m^2 for the chaser and target spacecraft, respectively. The Solar and Lunar data were provided by NASA's Jet Propulsion Laboratory Horizons website based off measurements made on July 1, 2018.[1]

The osculating orbital elements for the first and second cases (HEO) examples are initialized as $a = 60000$ km, $e = 0.88$, $i = 92°$, $\omega = 270°$, $\Omega = 84°$, and $\theta = 0°$ for both spacecraft. The semi-major axis a and eccentricity e were selected such that the distance of the spacecraft $|\vec{r}|$ varies from a perigee of 7200 km to an apogee of 112 800 km. The LQR controller was initialized with

$$\boldsymbol{Q} = 10^{10}\boldsymbol{I}_6 \qquad \boldsymbol{R} = 10^{12}\boldsymbol{I}_3 \tag{70}$$

where $\boldsymbol{Q}$ and $\boldsymbol{R}$ are positive-definite weighting matrices [40]. This resulted in the following initial gains

$$\boldsymbol{K}_0 = \begin{bmatrix} 0.1000 & 0 & 0 & 0.4583 & 0 & 0 \\ 0 & 0.1000 & 0 & 0 & 0.4583 & 0 \\ 0 & 0 & 0.1000 & 0 & 0 & 0.4583 \end{bmatrix} \tag{71}$$

Using the initial set of gains calculated with LQR, the gain calculation procedure shown in Section 2.3 resulted in the following gain functions (as a function of β)

$$K_p = \begin{bmatrix} 45768.3013 & 0.1000 \end{bmatrix} \begin{bmatrix} \beta & 1 \end{bmatrix}^T \in \beta = [0, 0.0669] \tag{72}$$

$$K_d = \begin{bmatrix} 45768.3013 & 0.4583 \end{bmatrix} \begin{bmatrix} \beta & 1 \end{bmatrix}^T \in \beta = [0, 0.0669] \tag{73}$$

[1] https://ssd.jpl.nasa.gov/horizons.cgi.

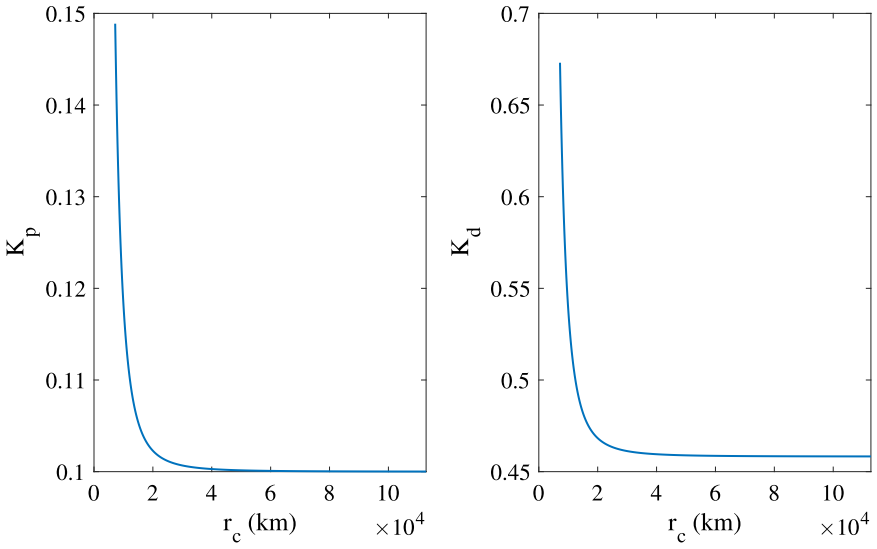

Fig. 3. PD gains as a function of distance of the chaser from the earth.

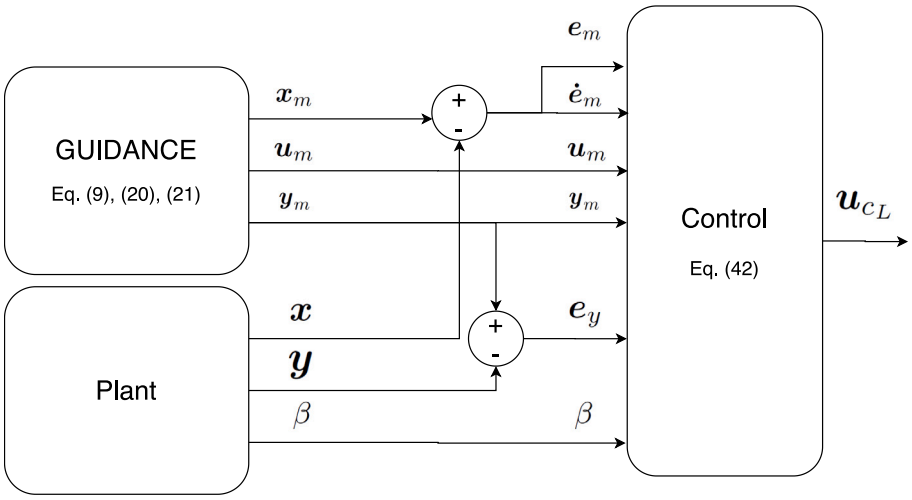

Fig. 4. Block scheme diagram of the GSAC guidance and control architecture.

such that the eigen-values of the closed-loop system remain within the region bounded by $\alpha = -0.2291$, $\zeta = 0.7245$ and $\omega_n = 0.3162$. The interval for the parameter β implies that the calculated gain functions remain guarded for all values contained within that interval. In other words, the controller is robust to changes in the distance of the spacecraft from the primary body as well as distances of the third-body with respect to the primary body. The previously calculated gain functions are applicable to any arbitrary orbit as long as the values for orbital radius of the spacecraft and the third body that determines the parameter β never exceeds 0.0669. Fig. 3 shows how the controller gains vary as a function of distance from the Earth.

The GSAC feedforward adaptation rates were initialized, with trial and error, as

$$\begin{aligned} \Gamma_{Px} &= 10^{-5}\boldsymbol{I}_6 \quad \Gamma_{Pu} = 10^{-5}\boldsymbol{I}_3 \\ \Gamma_{Ix} &= 10^{-6}\boldsymbol{I}_6 \quad \Gamma_{Iu} = 10^{-6}\boldsymbol{I}_3 \end{aligned} \tag{74}$$

with $\lambda = 0.5$. The relative position error, $\boldsymbol{e}_m$, is defined as the difference, in the LVLH reference frame, between the desired (ideal) relative motion and numerical propagator output. Fig. 4 shows a block-scheme diagram of the GSAC guidance and control architecture.

5.1. Case 1: Guidance comparison

The proposed guidance and control system was evaluated for an in-plane elliptical formation using Eq. (9) as an ideal model and compared against using Hill's equations in Figs. 5–10. Figs. 5 and 6 show the relative motion in LVLH using Eq. (9) and Hill's equations, respectively while Figs. 7–10 show the required control accelerations. Observing the Figures, during perigee passage at the beginning of every orbit (at $t = 0, 1.5, 3 \times 10^5$ s), spikes in control actuation and error occur. By comparison the in-plane elliptical formation using Hill's equations demanded a significantly larger control input (ten times larger in the radial and along-track directions).

5.2. Case 2: G&C comparison on HEO

The second case, initialized with the same target orbital elements as the first case, tests the performance of the proposed Guardian Map-based simple adaptive control law (GSAC) against a standard LQR controller that widely used in literature for formation flight. In addition, the proposed control law of Eq. (42) was tested with the adaptive feed-forward gains set to zero such (i.e.: a stand alone Guardian Map PD Controller, denoted by Gmap within the results). Specifically, the

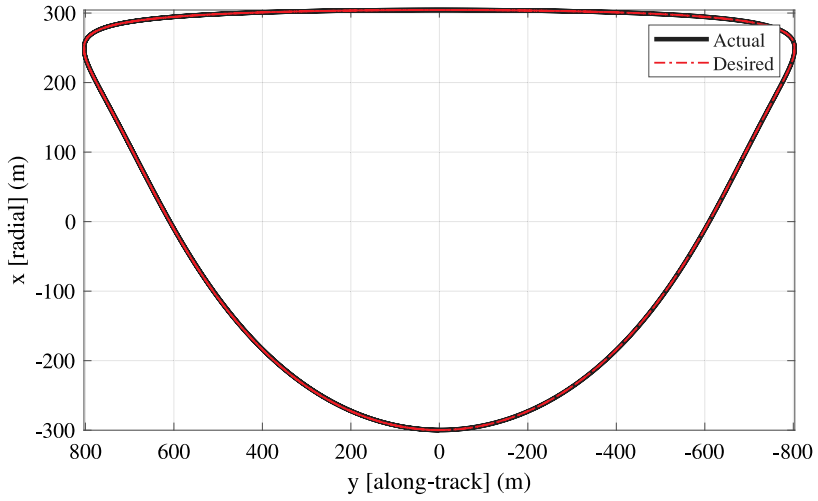

Fig. 5. In-plane elliptical formation using Eq. (9) and GSAC.

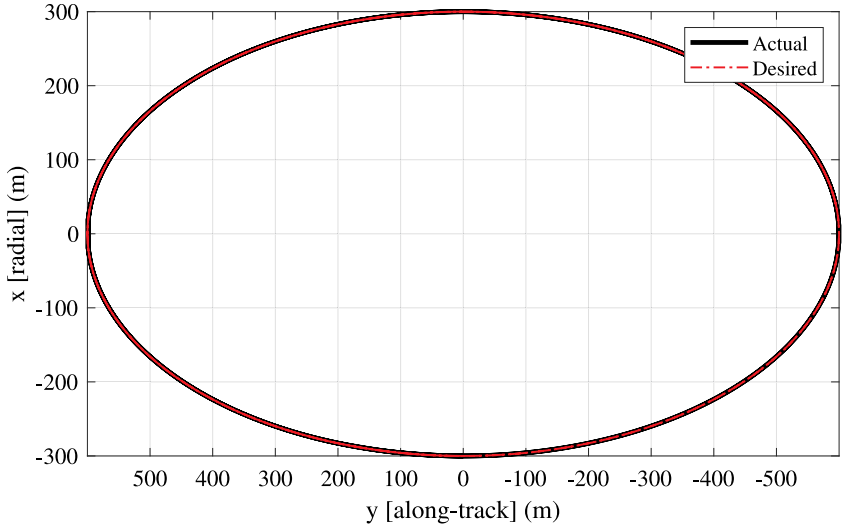

Fig. 6. In-plane elliptical formation using Hill's equations and GSAC.

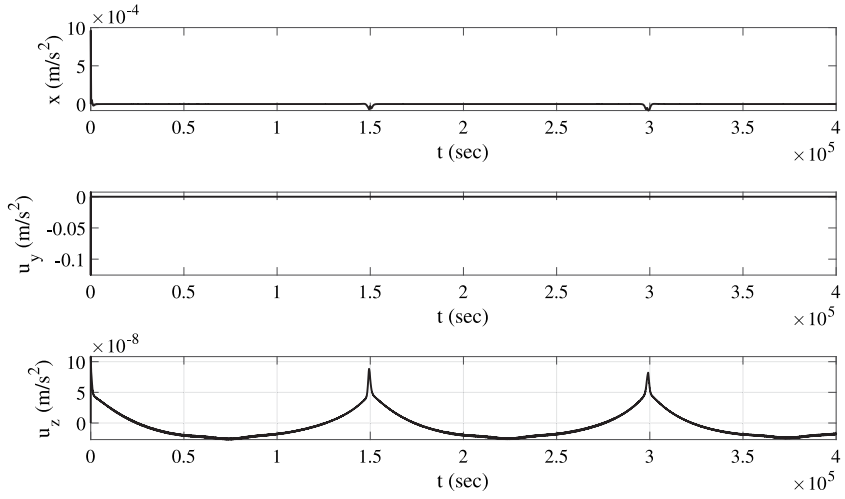

Fig. 7. GSAC in-plane elliptical formation control accelerations $\boldsymbol{u}_{c_L} = \begin{bmatrix} x & y & z \end{bmatrix}$ using Eq. (9).

LQR controller is initialized with the same $\boldsymbol{Q}$ and $\boldsymbol{R}$ matrices as the Guardian map initial gain selection.

Fig. 11 shows the desired and actual relative motion in LVLH using the three control methods when the chaser is commanded to follow

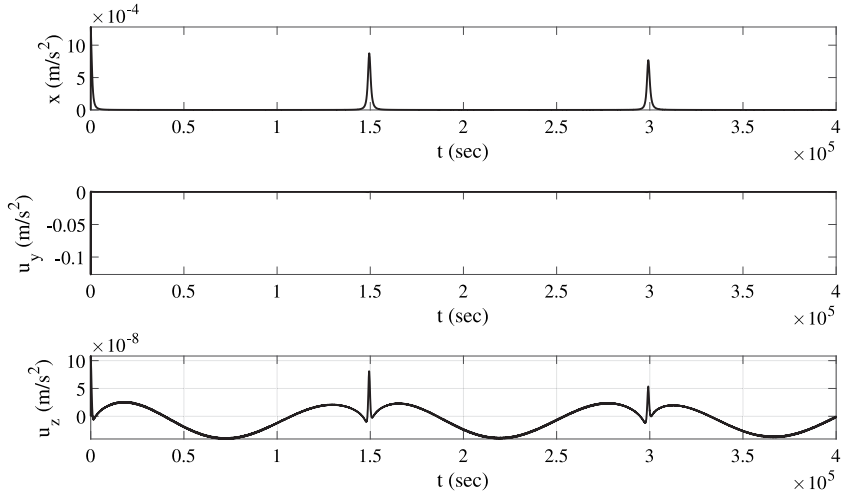

Fig. 8. GSAC in-plane elliptical formation control accelerations $\boldsymbol{u}_{c_L} = \begin{bmatrix} x & y & z \end{bmatrix}$ using Hill's equations.

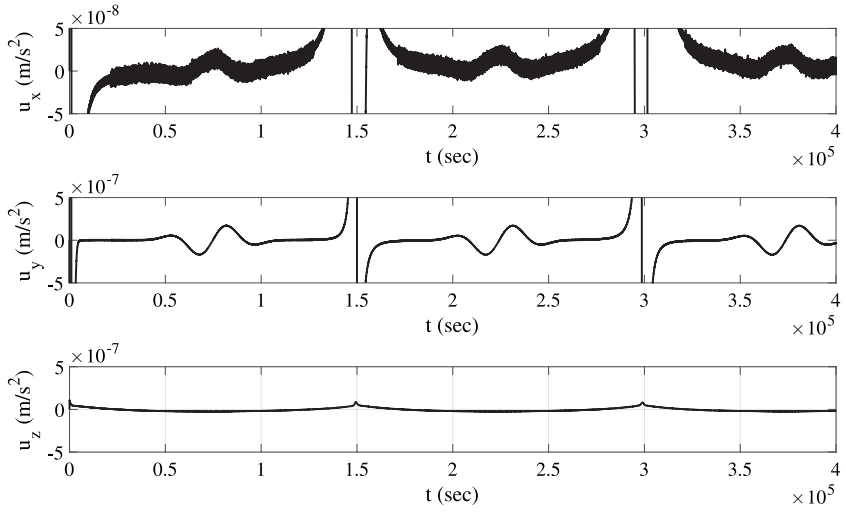

Fig. 9. GSAC in-plane elliptical formation control accelerations $\boldsymbol{u}_{c_L} = \begin{bmatrix} x & y & z \end{bmatrix}$ (Magnified) using Eq. (9).

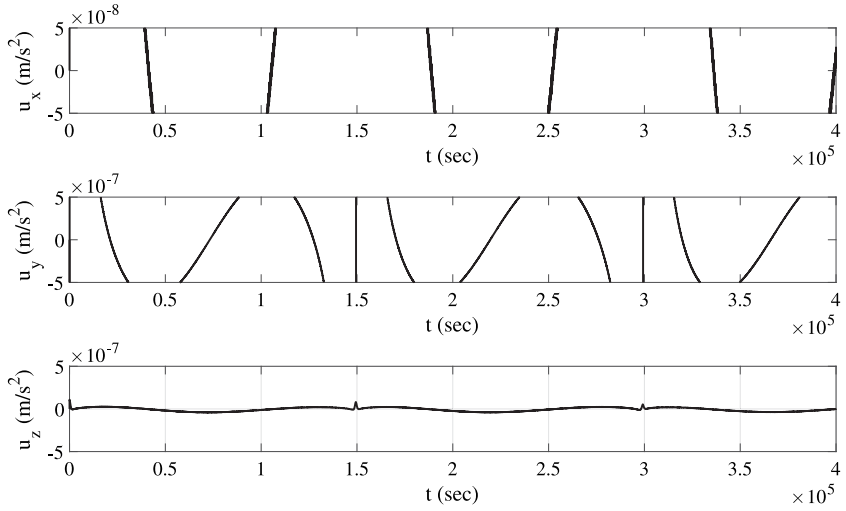

Fig. 10. GSAC in-plane elliptical formation control accelerations $\boldsymbol{u}_{c_L} = \begin{bmatrix} x & y & z \end{bmatrix}$ (Magnified) using Hill's equations.

a relative trajectory defined by $\Delta\boldsymbol{oe} = \begin{bmatrix} 0 & 0 & 0 & 0 & 0.01^\circ & -0.01^\circ \end{bmatrix}$ with an initial offset in the along-track direction of 1 km. Fig. 12 show the control accelerations using the three different guidance and control architectures while Fig. 13 show the relative distances and position

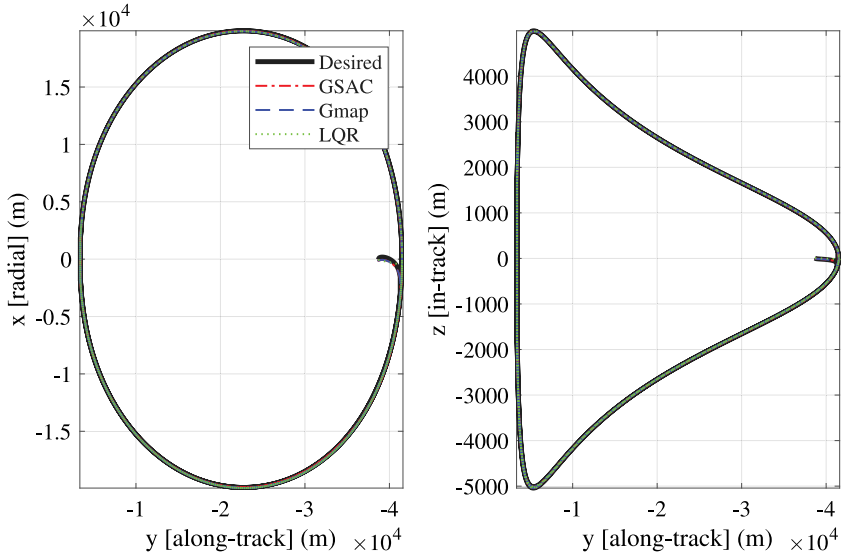

Fig. 11. Case 2: Relative motion in LVLH.

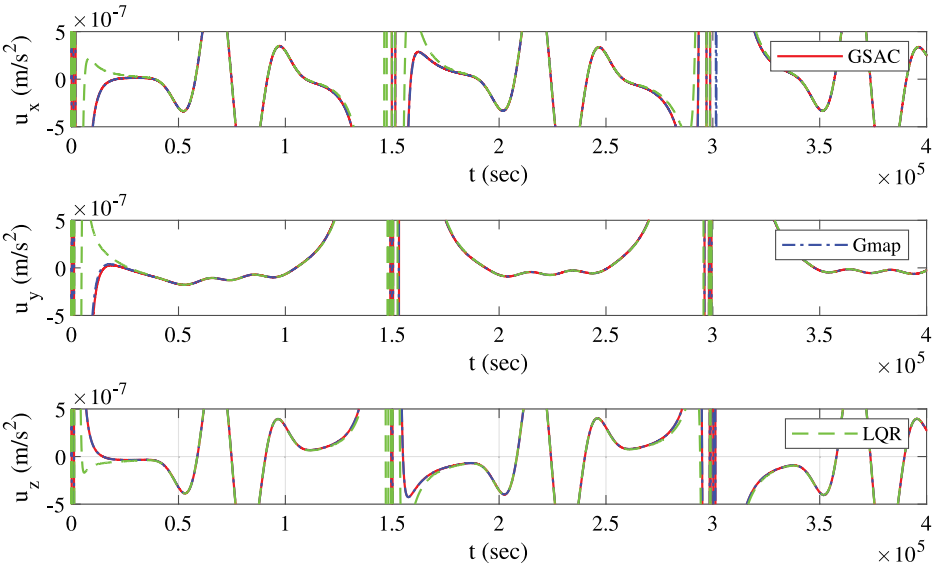

Fig. 12. Case 2: Control accelerations in LVLH.

errors. By observing the results, it can clearly be seen that, compared to LQR, the Guardian Map based control law exhibits better tracking performance while using slightly less control input, with the feed-forward adaptation law providing further improvement in tracking performance when compared to the Guardian Map only strategy. In addition, when comparing the proposed guidance and control law against the LQR controller, the initial errors and control input associated with the offset are significantly less. Specifically, the initial controller inputs for the Guardian Map method are on the order of one-hundred times less when compared to the LQR controller. The proposed GSAC control law, due to the presence of feed-forward gains, reduced the errors bringing them asymptotically to zero over the most part of the relative motion when compared to the standalone Guardian Map controller. However, specifically at the points of closest approach, the tracking errors for radial (x) and cross-track (z) directions of the GSAC controller increased slightly to match the standalone Guardian Map errors.

Fig. 14 shows the transient response in the beginning of the simulation of control accelerations and errors. The Guardian Map controller resulted in a decrease in error and oscillations at the points of closest approach as opposed to the LQR controller. In addition, the guardian map controller settled in less than 100 s while the errors for the LQR took even longer to setter, eventually resulting in a greater steady state error when also comparing with Fig. 13. The transient response of the GSAC law was observed to be similar to the case without the feed-forward gains, which is expected, since the feed-forward gains are responsible for bringing the errors asymptotically to zero after the transients have died out.

Fig. 15 shows the response of the controller inputs and errors at perigee, where the inertial velocity of the spacecraft are highest. The Guardian Map controllers, including the proposed GSAC controller, required slightly more control input, but reduced the tracking errors to near zero when compared to the LQR controller. This demonstrates the robustness of the Guardian Map control law to disturbances caused by the orbit's eccentricity.

5.3. Proba-3

For the Proba-3 case, the chaser spacecraft is assumed to start at the origin (i.e.: attached to the target) such that the osculating

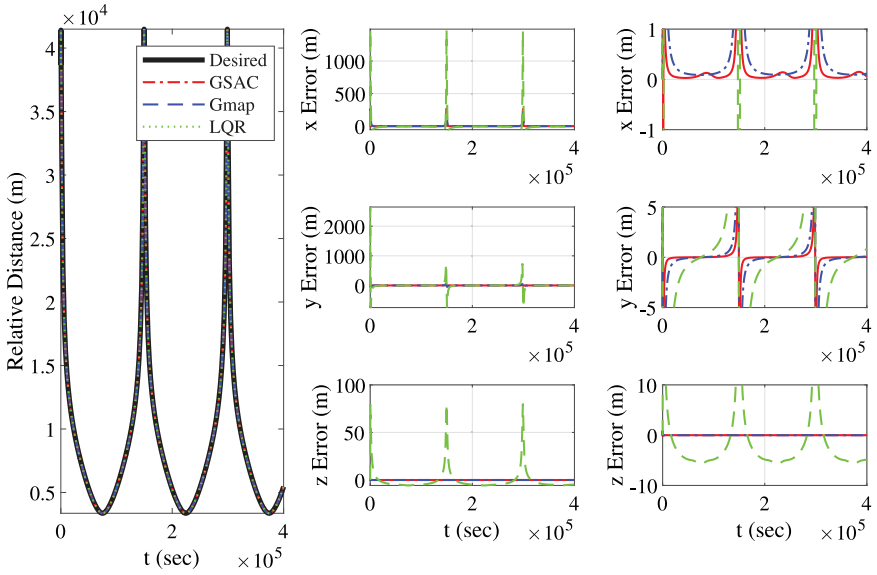

Fig. 13. Case 2: Relative distances and errors in LVLH.

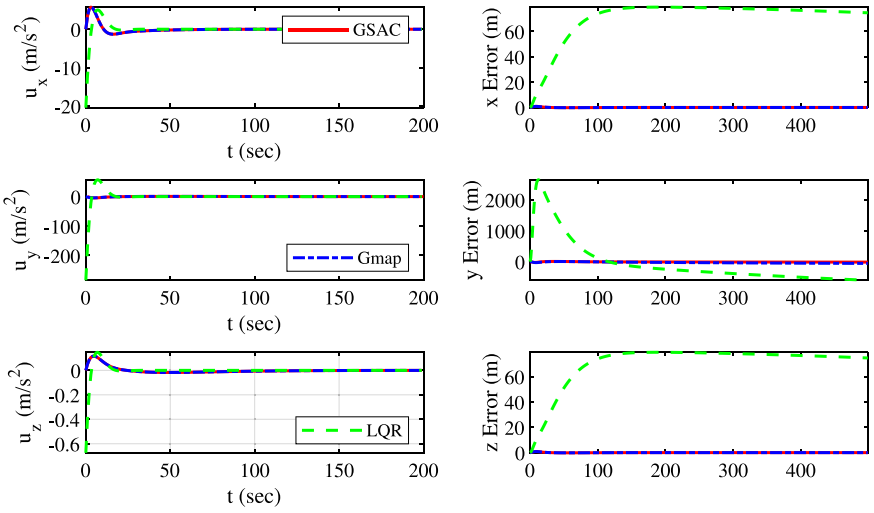

Fig. 14. Case 2: Transient responses in LVLH.

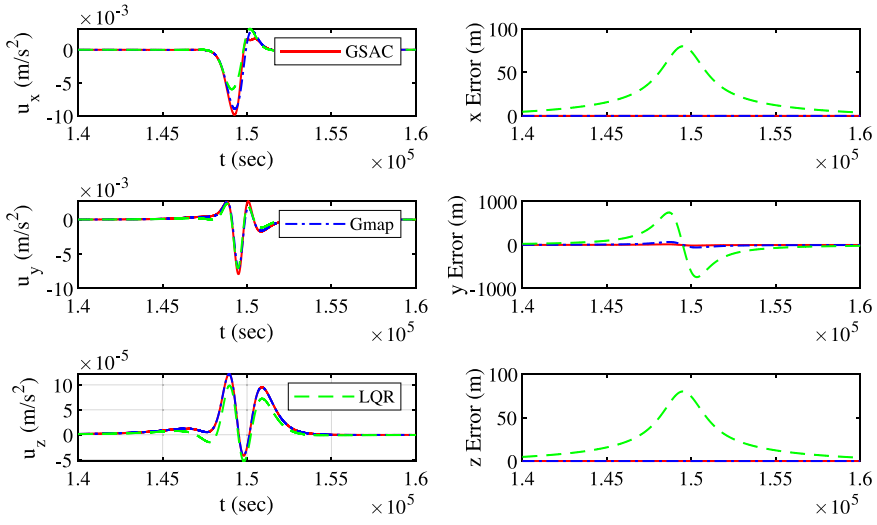

Fig. 15. Case 2: Response at perigee in LVLH.

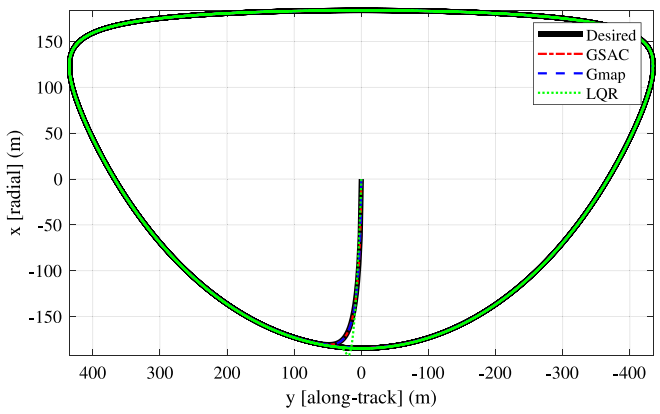

Fig. 16. Proba-3: Relative motion in LVLH.

orbital elements for both spacecraft are initialized as $a = 36944$ km, $e = 0.811$, $i = 59.0°$, $\omega = 188°$, $\Omega = 84.0°$, and $\theta = 0°$ [39]. The controller was commanded to track a relative trajectory defined by $\Delta\boldsymbol{oe} = \begin{bmatrix} 0 & 5\times10^{-6} & 0 & 0 & 0 & 0 \end{bmatrix}$, which is an approximation of the trajectory Proba-3 is expected to have [27]. Figs. 16–20 show that the Guardian Map based control law remains robust and fuel efficient for a different type of HEO. Furthermore, both Guardian Map-based controllers displayed better transient and steady-state performance than the LQR controller tuned for the Proba-3 mission initial conditions with the same $\boldsymbol{Q}$ and $\boldsymbol{R}$ matrices as the first two cases.

5.4. Alouette-2

For the LEO case, the osculating orbital elements for a fictitious mission around Alouette-2 was initialized as $a = 7947$ km, $e = 0.134$, $i = 79.8°$, $\omega = 151.9°$, $\Omega = 348.3°$, and $\theta = 40°$. Figs. 21–25 shows the results for when the chaser is commanded to follow a relative trajectory defined by $\Delta\boldsymbol{oe} = \begin{bmatrix} 0 & 5\times10^{-5} & 0.01° & 0 & 0 & 0 \end{bmatrix}$ with an initial offset in the radial direction of −5 km. When comparing the results to the observations made in the previous section, the example presented in this section demonstrates that the proposed GSAC and Guardian Map PD laws remain robust an applicable to various orbital conditions including LEO and HEO.

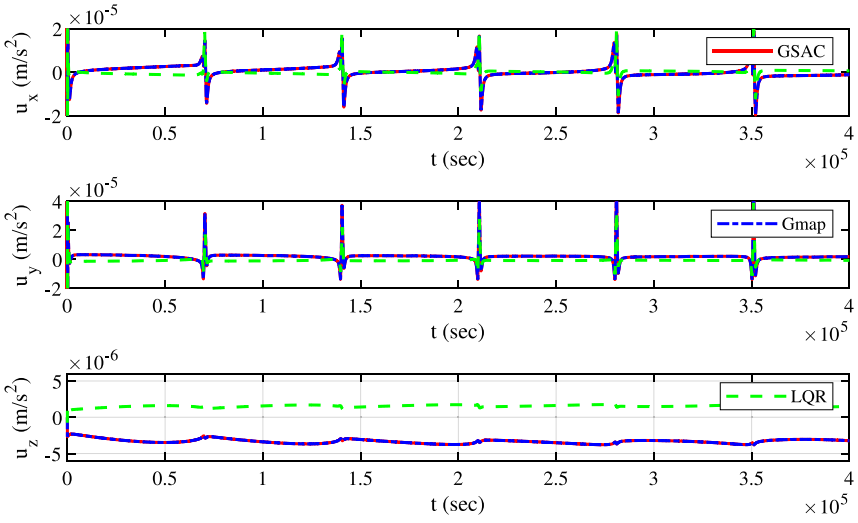

Fig. 17. Proba-3: Control accelerations in LVLH.

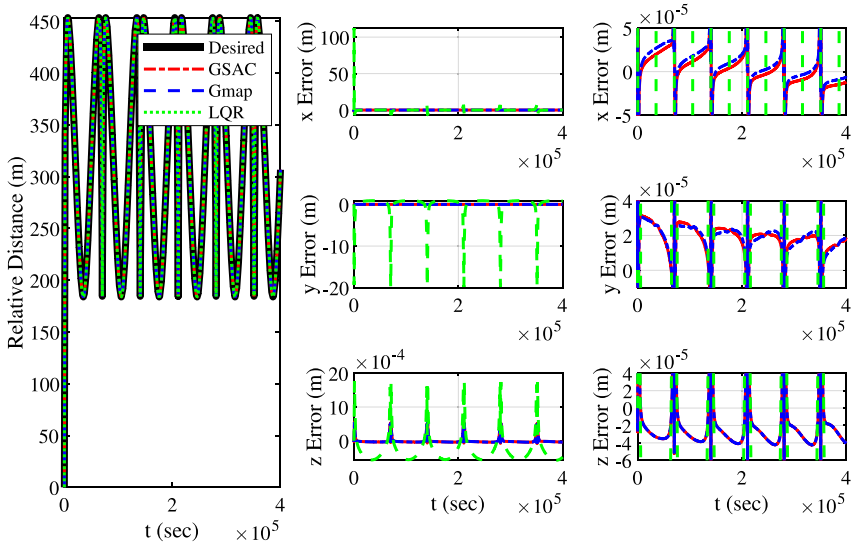

Fig. 18. Proba-3: Relative distances and errors in LVLH.

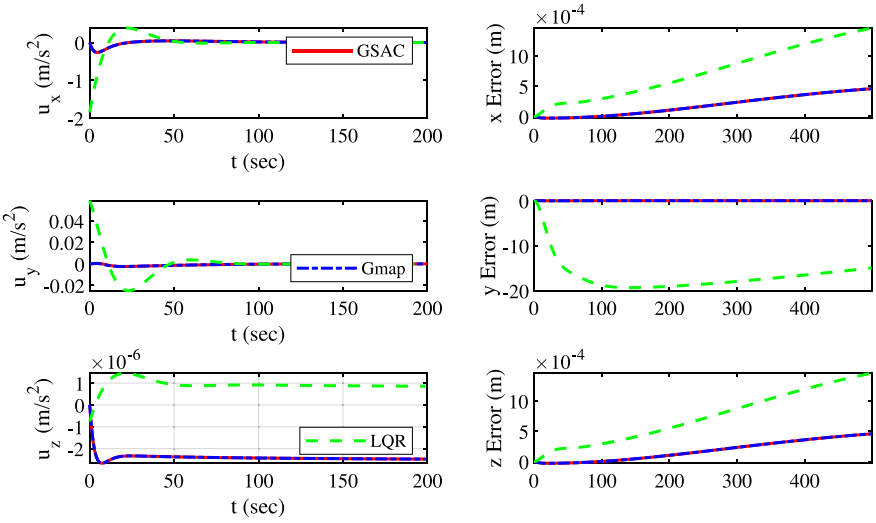

Fig. 19. Proba-3: Transient responses in LVLH.

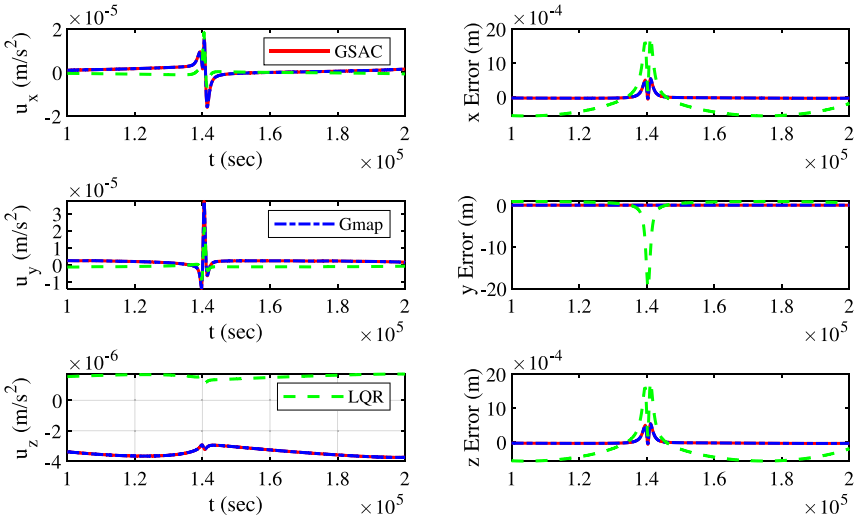

Fig. 20. Proba-3: Response at perigee in LVLH.

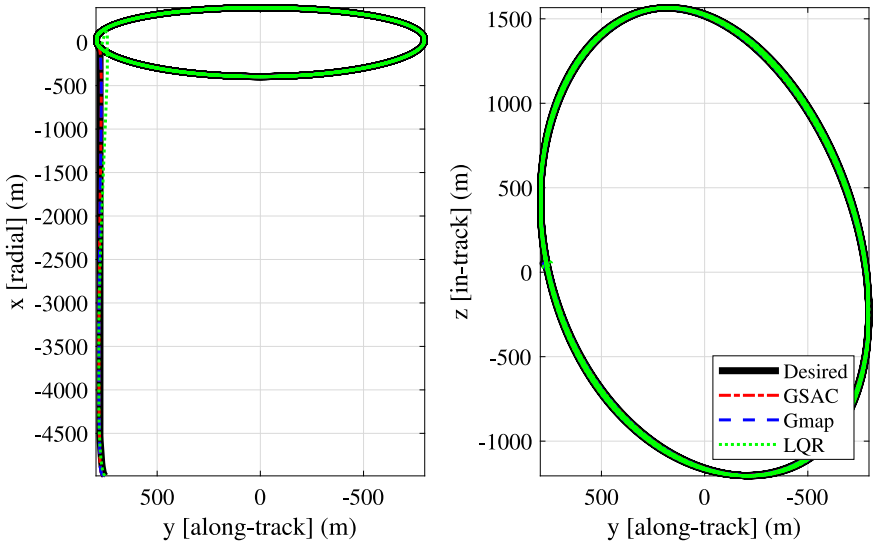

Fig. 21. Alouette-2: Relative motion in LVLH.

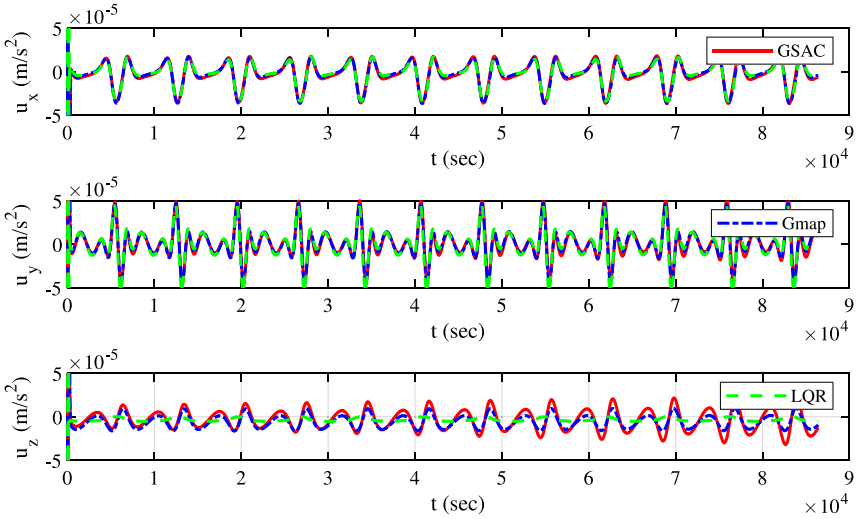

Fig. 22. Alouette-2: Control accelerations in LVLH.

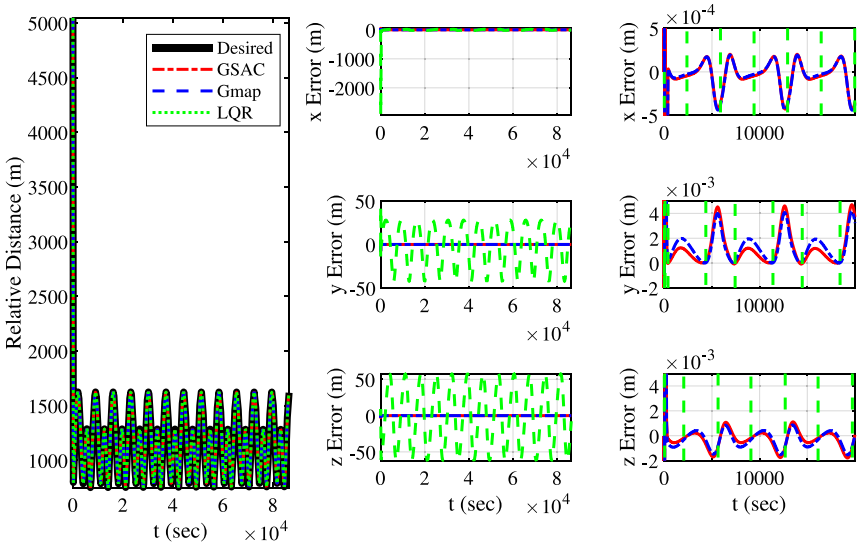

Fig. 23. Alouette-2: Relative distances and errors in LVLH.

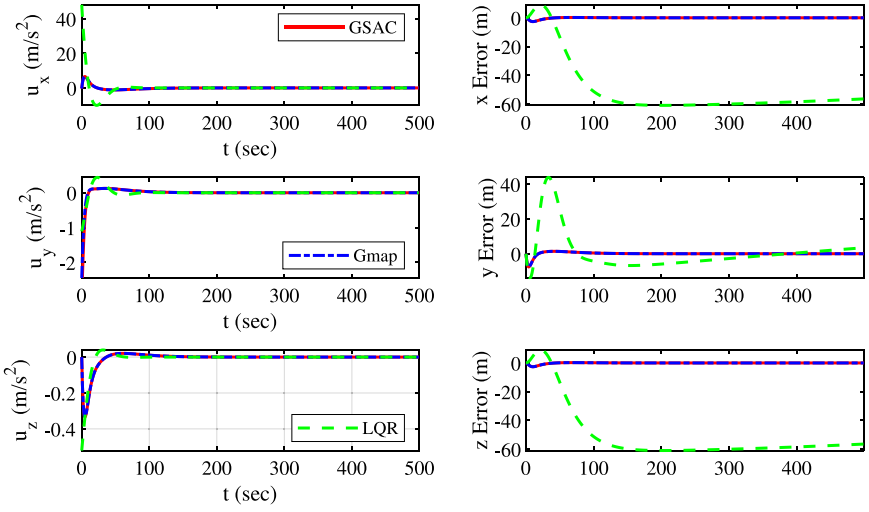

Fig. 24. Alouette-2: Transient responses in LVLH.

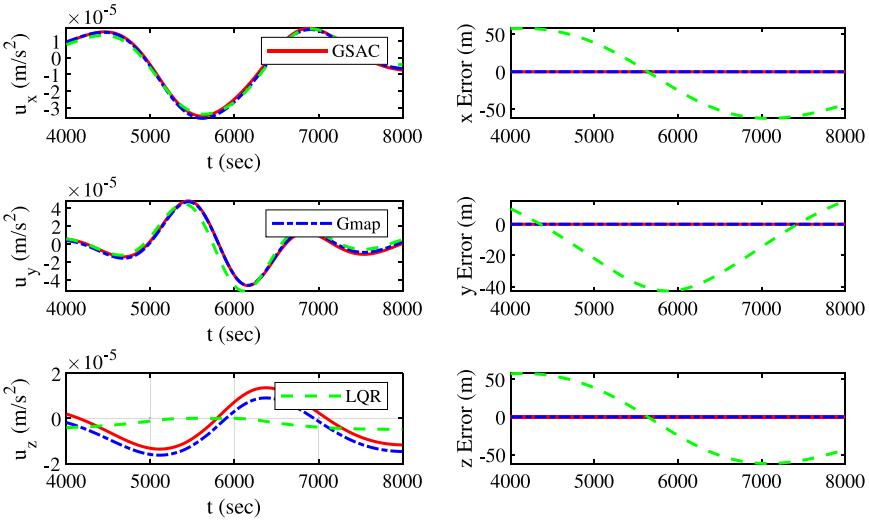

Fig. 25. Alouette-2: Response at perigee in LVLH.

Table 1
Total cost (Delta-V) in [m/s] for each guidance method (Case 1).

Guidance	Cost
Hill's $J(u)$	0.007875
ROE $J(u)$	0.001842

Table 2
Total cost (Delta-V) in [m/s] for each control method.

G&C Method	GSAC	Guard Map PD	LQR
Case 2 $J(u)$	0.1988	0.1983	1.1209
Proba-3 $J(u)$	0.0089	0.0089	0.0208
Alouette-2 $J(u)$	0.1735	0.1733	0.5086

5.5. Cost function analysis

This subsection presents an analysis of control energy in terms of delta-v for the three different control methodologies. The cost function $J(u)$ is selected as

$$J(u) = \int_0^T \left(|u_x| + |u_y| + |u_z|\right) dt \approx \Delta t \sum_{t=0}^{T} \left(|u_x| + |u_y| + |u_z|\right) \tag{75}$$

where Δt denotes simulation time-step, which is equal to one second for all cases tested. This cost function is also equivalent to the area under the acceleration versus time graphs, or in other words, the total delta-v used by the chaser throughout the simulation period.

Table 1 shows the cost for the simulations testing Hill's equations versus the relative orbital elements (ROE) based equations represented by Eq. (9).

The results presented by Table 1 clearly show the reduced energy cost of using relative orbital elements as a guidance solution to create natural bounded trajectories.

Table 2 shows the total cost for each of the control methodologies applied to three different initial conditions, as presented in the previous subsections. Overall, the GSAC control law demanded slightly more control energy in terms of delta-v than the Guardian Map PD; however, the control energy was considerably less ranging from nearly three quarters for the Alouette-2 case the delta-v required to almost an order of magnitude less for case 2 and Proba-3. This demonstrates the increase in performance of the proposed control law. In addition, the control energy required for case-2 and Alouette-2 is considerably more than Proba-3 because of the larger separation distances involved.

6. Conclusion

This paper presented a novel method of ensuring robust stability of spacecraft formation flying controllers. A new linear parameter-varying model in terms of a parameterized set of polynomial matrices that incorporates the simplified effects of a third-body was formulated enabling the use of Guardian Map theory. Using the newly developed model and by combining Guardian Map theory with Simple Adaptive Control theory, a new hybrid control law that is applicable to arbitrary eccentric orbits was derived resulting in the guaranteed asymptotic convergence of states. Furthermore, the use of Guardian Map theory ensures that the proposed control law is robust to changes in orbital position of the chaser spacecraft with respect to a primary body.

A guidance method using ideal states as the desired states with natural bounded relative trajectories in terms of relative orbital elements is proposed. The guidance law takes advantage of state–space modeling combined with damping ratio and natural frequency obtained using the Guardian Map theory to determine the ideal reference trajectory used in the proposed control architecture.

The new method was then validated against a numerical simulator that included effects of drag, third body and gravitational field. The natural trajectories yielded significantly lower control demand while demonstrating an increase in tracking performance when compared to commanding the chaser to follow an unnatural relative trajectory. When the newly developed control law was compared to a standard LQR controller, the relative motion yielded significantly lower errors and lower control actuation.

Declaration of competing interest

The authors declare that they have no known competing financial interests or personal relationships that could have appeared to influence the work reported in this paper.

References

[1] Intelsat 901 satellite returns to service using northrop grumman's mission extension vehicle, 2020, https://news.northropgrumman.com/news/releases?c=28198 (accessed: 2020-08-05).
[2] G. Hill, Researches in the lunar theory, Amer. J. Math. 1 (1878) 5–26.
[3] A. Moccia, A. Renga, Distributed Space Missions for Earth System Monitoring, Springer–Verlag, New York, 2013.
[4] J.K. Eyer, C. Damaren, R.E. Zee, E. Cannon, A formation flying control algorithm for the canx-4 & 5 low earth orbit nanosatellite mission, Space Technol. 27 (4) (2007) 147–158.

[5] D. Stansbery, J. Cloutier, Nonlinear control of satellite formation flight, in: AIAA Guidance, Navigation, and Control Conference and Exhibit, 2012, http://dx.doi.org/10.2514/6.2000-4436.
[6] R. Kristiansen, P.J. Nicklasson, Spacecraft formation flying: A review and new results on state feedback control, Acta Astronaut. 65 (11) (2009) 1537–1552, http://dx.doi.org/10.1016/j.actaastro.2009.04.014.
[7] M. Queiroz, V. Kapila, Q. Yant, Adaptive nonlinear control of multiple spacecraft formation flying, J. Guid. Control Dyn. 23 (2000) 385–390, http://dx.doi.org/10.2514/2.4549.
[8] H. Wong, V. Kapila, A.G. Sparks, Adaptive output feedback tracking control of spacecraft formation, Internat. J. Robust Nonlinear Control 12 (23) (2002) 117–139, http://dx.doi.org/10.1002/rnc.679.
[9] S. Ulrich, Nonlinear passivity-based adaptive control of spacecraft formation flying, in: American Control Conference (ACC), 2016, pp. 7432–7437, http://dx.doi.org/10.1109/ACC.2016.7526846.
[10] S. Ulrich, J. Sasiadek, Decentralized simple adaptive control of nonlinear systems, Int. J. Adapt. Control Signal Process. 28 (2013) http://dx.doi.org/10.1002/acs.2446.
[11] D. Saussie, O. Akhrif, C. Bérard, L. Saydy, Longitudinal flight control synthesis with guardian maps, in: AIAA Guidance, Navigation, and Control Conference and Exhibit, 2012, http://dx.doi.org/10.2514/6.2009-5988.
[12] D. Saussie, O. Akhrif, L. Saydy, Aircraft pitch rate control design with guardian maps, in: 18th Mediterranean Conference on Control and Automation, MED'10 - Conference Proceedings, 2010, http://dx.doi.org/10.1109/MED.2010.5547842.
[13] S.-J. Chen, S.-P. Yang, L.-G. Shiau, Guardian map approach to robust stability of interval systems, Internat. J. Systems Sci. 43 (12) (2012) 2193–2201, http://dx.doi.org/10.1080/00207721.2012.659700.
[14] G. Ghazi, R. Botez, Lateral control design for the cessna citation x with robustness and handling qualities requirements, in: 62nd CASI Aeronautics Conference and AGM, Montreal, Quebec.
[15] L. Mengying, S. Zhiyong, X. Dibo, L. Yanbin, L. Delin, Adaptive control of hypersonic vehicles using guardian maps theory, in: 2015 34th Chinese Control Conference (CCC), 2015, pp. 5653–5657, http://dx.doi.org/10.1109/ChiCC.2015.7260522.
[16] D. Xiao, M. Liu, Y. Liu, Y. Lu, Switching control of a hypersonic vehicle based on guardian maps, Acta Astronaut. 122 (2016) 294–306, http://dx.doi.org/10.1016/j.actaastro.2016.02.017.
[17] X. Dibo, C. Boyi, Y. Liu, L. Mengying, L. Yuping, A design method of switching control for hypersonic vehicles based on guardian maps, in: 34th Chinese Control Conference (CCC), 2015, pp. 5658–5662, http://dx.doi.org/10.1109/ChiCC.2015.7260523.
[18] V. Dubanchet, D. Saussie, C. Bérard, L. Saydy, R. Gourdeau, Robust control of a launch vehicle in atmospheric ascent based on guardian maps, in: Proceedings of the American Control Conference, 2012, pp. 938–943, http://dx.doi.org/10.1109/ACC.2012.6315316.
[19] G. Inalhan, M. Tillerson, J. How, Relative dynamics and control of spacecraft formations in eccentric orbits, J. Guid. Control Dyn. 25 (1) (2002) 48–59, http://dx.doi.org/10.2514/2.4874.
[20] L. Saydy, A. Tits, E. Abed, Guardian maps and the generalized stability of parametrized families of matrices and polynomials, Math. Control Signals Syst. 3 (1990) 345–371, http://dx.doi.org/10.1007/BF02551375.
[21] D. Saussié, L. Saydy, O. Akhrif, C. Bérard, Gain scheduling with guardian maps for longitudinal flight control, J. Guid. Control Dyn. 34 (4) (2011) 1045–1059, http://dx.doi.org/10.2514/1.52178.
[22] H. Schaub, J.L. Junkins, Analytical Mechanics of Space Systems, AIAA American Institute of Aeronautics & Astronautics, 2018, pp. 593–673.
[23] P. Gurfil, N.J. Kasdin, Nonlinear modeling of spacecraft relative motion in the configuration space, J. Guid. Control Dyn. 27 (1) (2004) 154–157, http://dx.doi.org/10.2514/1.9343.
[24] P. Gurfil, K.V. Kholshevnikov, Manifolds and metrics in the relative spacecraft motion problem, J. Guid. Control Dyn. 29 (4) (2006) 1004–1010, http://dx.doi.org/10.2514/1.15531.
[25] Y. Chihabi, S. Ulrich, Analytical spacecraft formation dynamics in eccentric orbits with gravitational, drag and third body perturbations, in: 29th AAS/AIAA Space Flight Mechanics Meeting, Ka'anapali, HI, 2019.
[26] Y. Chihabi, S. Ulrich, Spacecraft formation guidance law using a state transition matrix with gravitational, drag and third-body perturbations, in: 30th AIAA/AAS Space Flight Mechanics Meeting, Orlando, FL, 2020.
[27] B. Kuiack, S. Ulrich, Nonlinear analytical equations of relative motion on J2-perturbed eccentric orbits, AIAA J. Guid. Control Dyn. 41 (11) (2017) 2666–2677, http://dx.doi.org/10.2514/1.G003723.
[28] Appendix a: Newton–Raphson Method, John Wiley & Sons, Ltd, 2003, URL https://onlinelibrary.wiley.com/doi/abs/10.1002/0471458546.app1.
[29] O. Montenbruck, E. Gill, Satellite Orbits: Models, Methods, and Applications, Springer, 2001.
[30] H. Kaufman, I. Barkana, K. Sobel, Direct Adaptive Control Algorithms: Theory and Applications, second ed., in: Communications and Control Engineering Series, Springer, New York, NY, 1997.
[31] S. Ulrich, J.Z. Sasiadek, I. Barkana, On a new class of direct adaptive output feedback controllers for nonlinear square systems, in: 51st IEEE Conference on Decision and Control, IEEE, Piscataway, NJ, 2012, pp. 4139–4144.
[32] J. Slotine, W. Li, Applied Nonlinear Control, Prentice Hall, Englewood Cliffs, NJ, 1991.
[33] J. LaSalle, Stability of nonautonomous systems, Nonlinear Anal. TMA 1 (1) (1976) 83–90, http://dx.doi.org/10.1016/0362-546X(76)90011-0.
[34] I. Barkana, The new theorem of stability - direct extension of lyapunov theorem, Math. Eng. Sci. Aerosp. MESA 6 (2015) 519–535.
[35] G. Petit, B. Luzum, Iers Conventions, Tech. Rep., Verlag des Bundesamts für Kartographie und Geodäsie, Frankfurt am Main, 2010.
[36] A.F.B.A. Prado, Third-body perturbation in orbits around natural satellites, J. Guid. Control Dyn. 26 (1) (2003) 33–40, http://dx.doi.org/10.1155/2008/763654.
[37] R.C. Domingos, R.V. deMoraes, A.F.B.D.A. Prado, Third-body perturbation in the case of elliptic orbits for the disturbing bodies, Math. Probl. Eng. (2008) http://dx.doi.org/10.1155/2008/763654.
[38] D.A. Vallado, Fundamentals of Astrodynamics and Applications, second ed., Microcosm Press, El Segundo, CA, 2001, pp. 80–81.
[39] T.V. Peters, J. Branco, D. Escorial, L.T. Castellani, A. Cropp, Mission analysis for proba-3 nominal operations, Acta Astronaut. 102 (2014) 296–310, http://dx.doi.org/10.1016/j.actaastro.2014.01.010.
[40] F.L. Lewis, L. Xie, D. Popa, Optimal and Robust Estimation: With an Introduction to Stochastic Control Theory, second ed., CRC Press Taylor & Francis Group, 6000 Broken Sound Parkway NW, Suite 300 Boca Raton, FL, 2008, pp. 192–204, 33487-32742.